

Ba₃MIr₂O₉ hexagonal perovskites in the light of spin-orbit coupling and local structural distortionsAbhishek Nag,¹ Sayantika Bhowal,² F. Bert,³ A. D. Hillier,⁴ M. Itoh,⁵ Ilaria Carlomagno,⁶ C. Meneghini,⁶ T. Sarkar,⁷ R. Mathieu,⁷ I. Dasgupta,^{2,8} and Sugata Ray^{1,8,*}¹*Department of Materials Science, Indian Association for the Cultivation of Science, Jadavpur, Kolkata 700032, India*²*Department of Solid State Physics, Indian Association for the Cultivation of Science, Jadavpur, Kolkata 700032, India*³*Laboratoire de Physique des Solides, CNRS, Université Paris-Sud, Université Paris-Saclay, 91405 Orsay Cedex, France*⁴*ISIS Facility, Rutherford Appleton Laboratory, Chilton, Didcot, Oxon OX110QX, United Kingdom*⁵*Materials and Structures Laboratory, Tokyo Institute of Technology, 4259 Nagatsuta, Yokohama 226-8503, Japan*⁶*Dipartimento di Scienze, Università Roma Tre, Via della Vasca Navale 84, I-00146 Roma, Italy*⁷*Department of Engineering Sciences, Uppsala University, P.O. Box 534, SE-751 21 Uppsala, Sweden*⁸*Centre for Advanced Materials, Indian Association for the Cultivation of Science, Jadavpur, Kolkata 700032, India*

(Received 23 December 2017; revised manuscript received 31 January 2018; published 12 February 2018)

Spin-orbit coupling (SOC) is found to be crucial for understanding the magnetic and electronic properties of $5d$ transition metal oxides. In $5d$ systems, with Ir^{5+} ions, where ideally a nonmagnetic $J = 0$ ground state is expected to be stabilized in the presence of strong SOC, often spontaneous moments are generated due to hopping induced superexchange. This effect is more pronounced when the Ir atoms are close by, as in systems with Ir_2O_9 dimers in $6H$ $\text{Ba}_3\text{MIr}_2\text{O}_9$ compounds where magnetism is an outcome of complex Ir-O-Ir exchange paths, and is strongly influenced by the presence of local distortions. We find that subtle variations in the local structure of $\text{Ba}_3\text{MIr}_2\text{O}_9$ ($M = \text{Mg, Sr, and Ca}$) lead to markedly different magnetic properties. While SOC plays a pivotal role in explaining the insulating ground states of these systems, it is seen that $\text{Ba}_3\text{MgIr}_2\text{O}_9$, having a $P6_3/mmc$ symmetry, does not order down to low temperature despite having antiferromagnetic exchange interactions, while $\text{Ba}_3\text{CaIr}_2\text{O}_9$ shows weak dimer-like features and stabilizes in $C2/c'$ magnetic configuration with no net moment, and $\text{Ba}_3\text{SrIr}_2\text{O}_9$ possesses a ground state corresponding to the magnetic space group $C2'/c'$ and exhibits ferromagnet-like features.

DOI: [10.1103/PhysRevB.97.064408](https://doi.org/10.1103/PhysRevB.97.064408)**I. INTRODUCTION**

In the last few years, consideration of strong spin-orbit coupling (SOC) has been found to be crucial for explaining unexpected electronic and magnetic properties of $5d$ transition metal oxides (TMOs) [1–3]. The importance of SOC in determining the ground state of $5d$ systems lies in its increased strength with increasing atomic number, which allows it to split degenerate bands and effectively influence the electronic ground states. A rich phase diagram of properties predicted out of a competition between SOC and correlations in these heavy metal systems has led to the resurgence of $5d$ TMO research [4–6], beginning with the description of a novel Mott insulating state in layered tetravalent iridates (Ir^{4+} ; $5d^5$) [1]. This state arises in presence of strong SOC, which splits t_{2g} bands into a fully filled $j_{\text{eff}} = \frac{3}{2}$ quartet and a half filled narrow $j_{\text{eff}} = \frac{1}{2}$ doublet that further separates into occupied and unoccupied Hubbard bands in the presence of U [1–8]. Similarly, in pentavalent iridates (Ir^{5+} ; $5d^4$) as the crystal field splitting (Δ_{CFE}) dominates the Hund's exchange energy (J_H) of the $5d$ orbitals, a low spin state of $S = 1$ is realized in the absence of SOC. The projection of orbital angular momentum onto the degenerate t_{2g} orbitals gives an effective orbital angular momentum $L_{\text{eff}} = -1$ that couples with spin angular momentum S , producing ${}^6C_4 = 15$ possible many-body J states (four electrons in three degenerate t_{2g} orbitals each

allowing two spin orientations), with the $J = 0$ state having the lowest energy [9]. Understandably, pentavalent iridates hardly attracted any attention, as these systems are expected to display a nonmagnetic insulating ($M_J = 0$) $J = 0$ ground state [10]. Strangely, experimental realisation of this state seems to be non-trivial, as none of the reported $5d^4$ systems have shown this state so far [9,11–14]. It has often been stressed that the magnetism arises from singlet-triplet ($J = 0 \rightarrow J = 1$) excitations, which are made possible by distortions present in the IrO_6 octahedra producing local noncubic crystal fields ($\Delta_{\text{CFE}}^{\text{NC}}$) in these materials [11,15]. This is because both Δ_{CFE} and $\Delta_{\text{CFE}}^{\text{NC}}$ are found to reduce the influence of atomic SOC and therefore the $J = 0 \rightarrow J = 1$ gap [11,16–23]. But the most decisive factors against the observation of a nonmagnetic state are found to be the solid state effects, such as large bandwidth, that reduce the effective atomic SOC drastically, and the hopping induced superexchange mechanism producing magnetic moments [9,24–26].

$\text{Ba}_3\text{ZnIr}_2\text{O}_9$, a $6H$ hexagonal perovskite having Ir^{5+} ions, was found to be nearly nonmagnetic with a tiny moment of $0.26 \mu_B/\text{Ir}$ (ideal spin only moment: $2.83 \mu_B/\text{Ir}$) and, owing to a frustrated triangular network, a spin-orbital liquid state persisting down to 100 mK [9]. The small moments were shown to be generated due to hopping induced spin excitations between closely placed Ir^{5+} ions within Ir_2O_9 dimers [see Fig. 1(a)]. The net magnetism within such face-shared octahedra is a complicated outcome of different exchange interactions between the metal ions [23]. For example, one should take

*mssr@iacs.res.in

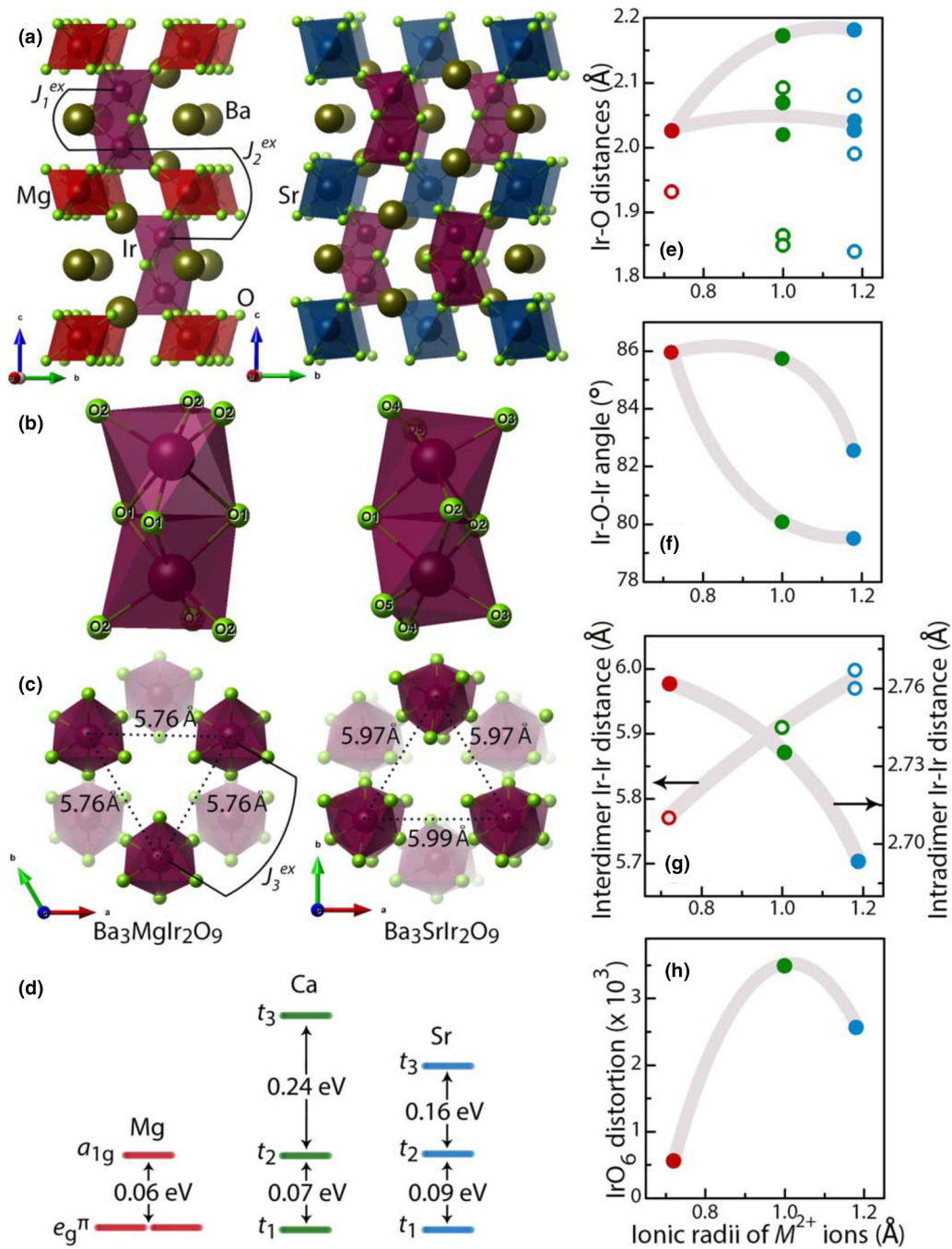


FIG. 1. (a) The crystal structures of Ba₃MgIr₂O₉ (left) and Ba₃(Ca/Sr)Ir₂O₉ (right) obtained from refinement. Intradimer and interdimer exchange interactions are also shown. Panel (b) shows the Ir₂O₉ dimers in the Mg and Sr systems with different O sites and (c) shows the Ir octahedra as seen on the *ab* plane. Ba₃CaIr₂O₉, which assumes the space group of Ba₃SrIr₂O₉, is not shown, and, being similar, they can be viewed interchangeably. (d) Splitting of the degenerate t_{2g} orbitals of the three compounds due to noncubic crystal field. (e) Variation of Ir-O bond distances as a function of M^{2+} ionic radii, with the solid symbols representing the Ir-O bonds between the two Ir’s in a dimer while the rest are the Ir-O’s directed away from the dimer. (f) Variation of Ir-O-Ir bond angles for the three systems. (g) Changes in interdimer and intradimer Ir-Ir distances with changing ionic radii of Mg, Ca, and Sr. (h) IrO₆ distortion values calculated for the three systems using structural refinement and FULLPROF [30].

into account the superexchanges mediated via three Ir-O-Ir paths within the face-shared Ir-O octahedra in the dimers [see Fig. 1(a)]. Direct Ir-Ir exchanges and local distortions affecting the Ir-O-Ir bond angles and bond lengths may further complicate the magnetic ground state of these systems by changing each of these exchange pathways. Khomskii *et al.*

recently reported the magnetic interactions expected for such face-shared octahedra having trigonal distortions for the d^5 configuration [23,27]. It is therefore of particular interest to study how SOC and distortion compete against each other to modify the magnetic properties of face shared systems having d^4 electrons. Hexagonal perovskites Ba₃MIr₂O₉ ($M = \text{Mg, Sr, Ca}$),

Sr, and Ca) have been reported to behave as paramagnets under externally applied strong magnetic fields [28]. It can be assumed that, as in Ba₃ZnIr₂O₉, in these systems too moments are generated due to hopping between the Ir⁵⁺ ions. Interestingly, subtle differences arise in the local structures of these compounds with increasing M²⁺ ionic radii ($\langle r \rangle_{\text{Mg}^{2+}} = 0.72 \text{ \AA}$, $\langle r \rangle_{\text{Zn}^{2+}} = 0.74 \text{ \AA}$, $\langle r \rangle_{\text{Ca}^{2+}} = 1.00 \text{ \AA}$, $\langle r \rangle_{\text{Sr}^{2+}} = 1.18 \text{ \AA}$) [29], which may have profound influence on their magnetic properties.

Here in this paper we show that, due to the presence of different degrees of octahedral distortions, a range of magnetic properties are found for the compounds Ba₃MIr₂O₉ ($M = \text{Mg, Sr, and Ca}$) from both theoretical calculations and experiments. A close structural resemblance of Ba₃MgIr₂O₉ (BMIO) to spin-orbital liquid Ba₃ZnIr₂O₉ ensures similar properties, such as featureless magnetic susceptibility, dominant antiferromagnetic (AFM) exchanges, and no sign of ordering down to 1.85 K. In spite of this, the minute difference in structures of Ba₃MgIr₂O₉ and Ba₃ZnIr₂O₉ is enough to influence the intradimer and interdimer exchanges and control the spin frustration. In comparison, due to monoclinic distortions in the lattices of Ba₃CaIr₂O₉ and Ba₃SrIr₂O₉ [see Fig. 1(a)] and release of frustration in the geometry, the magnetic signatures become prominent in low field magnetic susceptibility measurements. Due to strong octahedral distortions and different Ir-O-Ir angles breaking the inversion symmetry in these two systems, canting of spins give rise to noncollinear magnetic ground states. Ba₃CaIr₂O₉ shows a weak dimer-like feature in magnetic susceptibility, and theoretically a magnetic structure having AFM arrangement of net interdimer spins is found. For Ba₃SrIr₂O₉, a ferromagnet (FM) like upturn is observed in susceptibility congruent with the observation of net ferromagnetic moment as obtained from theory.

II. EXPERIMENTAL AND THEORETICAL METHODS

Polycrystalline Ba₃MIr₂O₉ ($M = \text{Mg, Ca, Sr}$) was synthesized by standard solid state reaction using stoichiometric amounts of BaCO₃, MgO, CaCO₃, SrCO₃, and IrO₂ as starting materials following an earlier report [28]. The final heating temperature of all the samples was 1200 °C. The sample purity was checked and structural parameters were obtained by refining powder x-ray diffraction measured in the Indian beamline (BL-18B) at the Photon Factory, KEK, Japan, and also using a laboratory based Bruker x-ray diffractometer. All the diffraction patterns obtained were refined by the Rietveld method using FULLPROF [30]. The structures shown in this paper were drawn using VESTA [31]. The x-ray photoelectron spectroscopy (XPS) measurements were carried out using a laboratory based Omicron electron spectrometer equipped with an EA125 analyzer, and also at the Material Science beamline, Elettra (Trieste, Italy). The electrical resistivity measurements were done in four-probe configuration in a laboratory based experimental setup. The DC magnetic measurements were carried out using a Quantum Design superconducting quantum interference device (SQUID) magnetometer. Heat capacities were measured using Quantum Design physical property measurement system (PPMS) at the Materials and Structural Laboratory, Tokyo Institute of Technology. Additional measurements were also done at Uppsala University,

Sweden. Muon spin relaxation (μSR) experiments were performed with the EMU spectrometer at the ISIS large scale facility in a helium flow cryostat. X-ray absorption spectra at the Ir L_3 edge were collected at Elettra, Trieste, Italy. The 11.1R-EXAFS beamline in standard transmission geometry at room temperature was employed to obtain extended x-ray absorption fine structure (EXAFS) spectra.

In order to study the electronic structure, density functional theory (DFT) calculations were performed using the plane-wave based projector augmented wave (PAW) [32,33] method as implemented in the Vienna *ab initio* simulation package (VASP) [34,35] within the generalized gradient approximation (GGA) including Hubbard U [36] and SOC. The kinetic energy cutoff of the plane wave basis was chosen to be 500 eV for all the compounds. Γ -centered $12 \times 12 \times 4$, $8 \times 5 \times 3$, and $8 \times 5 \times 3$ k meshes were used for the Brillouin-zone integration of the Ba₃MgIr₂O₉, Ba₃CaIr₂O₉, and Ba₃SrIr₂O₉ compounds respectively. All the calculations were performed with $U = 2$ eV and $J_H = 0.5$ eV at the Ir site unless stated otherwise. In order to have a quantitative estimate of the intradimer hopping strength and the noncubic crystal field within the Ir- t_{2g} levels, we employed the muffin-tin orbital (MTO) based N th order MTO (NMTO) [37–39] downfolding method as implemented in the Stuttgart code by constructing an Ir- t_{2g} only low energy Hamiltonian by integrating out the high energy degrees of freedom other than Ir- t_{2g} states.

III. RESULTS AND DISCUSSIONS

Powder x-ray diffraction (XRD) data collected from polycrystalline samples of Ba₃MIr₂O₉ ($M = \text{Mg, Ca, Sr}$) at room temperature confirm that all the compounds formed as reported earlier, without any impurity [28,40]. Satisfactory Rietveld refinement of the data was only possible with two different space groups for the samples. While the space group $P6_3/mmc$ with a higher symmetry could accommodate the smaller Mg²⁺ cation into the BaIrO₃ matrix, the larger cations Ca²⁺ and Sr²⁺ could form stable structures only within a lower symmetry space group $C2/c$ and a larger unit cell as shown in Fig. 1(a). Due to symmetry constraints, the Mg system has two types of O and, because of lowering of space group symmetry, the Ca/Sr systems have five different O sites as shown in Fig. 1(b) [40]. Thus there exist multiple Ir-O bond lengths in the IrO₆ octahedra in these compounds. The Mg system has two types of Ir-O bond lengths and, in the Ca/Sr systems, there are six different Ir-O bond lengths [Fig. 1(e)]. Consequently, there are multiple inequivalent Ir-O-Ir bond angles present in Ba₃CaIr₂O₉ and Ba₃SrIr₂O₉ [Fig. 1(f)] modifying the Ir-O-Ir exchange pathways, thereby creating the possibility of diverse magnetic properties in these compounds. In these two systems, the IrO₆ octahedra within the dimers are also rotated with respect to each other when seen from top of the ab plane [Fig. 1(c)]. The structural distortions are clearly visible for the Ca and the Sr perovskites with the O ions no longer aligned on top of each other along the c axis. Also, the frustrated equilateral triangular network of Ir ions present in Ba₃ZnIr₂O₉, which led it to a spin-orbital liquid state [9], is seen to be present in Ba₃MgIr₂O₉, but is replaced by an isosceles triangular network in the Ca and Sr systems, possibly reducing the frustration in these systems [Fig. 1(g)]. As one goes from Mg to

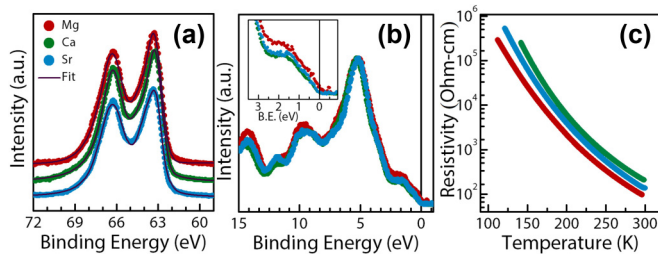


FIG. 2. (a) The XPS spectra for the Ir $4f$ core level, (b) the valence band photoemission spectra, and (c) four-probe electrical resistivity of polycrystalline $\text{Ba}_3\text{M}\text{Ir}_2\text{O}_9$ ($M = \text{Mg}, \text{Ca}, \text{Sr}$).

Sr, the interdimer Ir-Ir distance increases and at the same time the intradimer distance decreases, further reducing the chances of frustrated magnetism in $\text{Ba}_3\text{Ca}\text{Ir}_2\text{O}_9$ and $\text{Ba}_3\text{Sr}\text{Ir}_2\text{O}_9$. The details of the structural refinement are given in Supplemental Material (SM) [40]. Consequently, due to the presence of multiple Ir-O bond lengths, the Ir ions are acted upon by local noncubic crystal fields, resulting in nondegenerate t_{2g} orbitals. The calculated noncubic crystal field values for all the compounds using the NMTO downfolding technique are shown in Fig 1(d). The noncubic crystal field is found to be much stronger for the Ca compound compared to the Sr one, in agreement with the stronger distortion of the IrO_6 octahedra in the former [see Fig. 1(h)], as calculated using bond angle and bond length variance in FULLPROF [30]. The trigonal distortion of the face-shared IrO_6 octahedra in the hexagonal symmetry of the Mg compound splits the Ir- t_{2g} levels into a low-lying doublet (e_g^π) and a singlet (a_{1g}) with an energy separation of ~ 0.06 eV. On the other hand, monoclinic symmetry of the Ca and Sr compounds leads to much stronger distortion of the IrO_6 octahedra so that degeneracy of the t_{2g} orbitals is fully lifted.

Local atomic site disorder between the M^{2+} and Ir ions will result in corner sharing IrO_6 octahedra that may change overall magnetic properties in these systems [41]. To confirm that the local order is identical to the structure obtained from XRD, and the Ir ions sit only within the face-shared Ir_2O_9 dimers, we did EXAFS at the Ir L_3 edge. We used a multishell data fitting to get chemical order information from next neighbor coordination shell analysis [40,42]. The EXAFS data analysis confirms negligible chemical disorder ($< 1\%$) with local interatomic distances between Ir and M^{2+} ions comparable with XRD measurements for all the three compounds. Since corner-shared IrO_6 octahedra are absent, magnetism observed from experiments originates solely from face-shared Ir_2O_9 dimers.

The stoichiometric formula of $\text{Ba}_3\text{M}\text{Ir}_2\text{O}_9$ ($M = \text{Mg}, \text{Ca}, \text{Sr}$) suggests that Ir should be in the 5+ oxidation state. This oxidation state of Ir ions is of foremost importance in the realization of the $J = 0$, state especially because the presence of magnetic moments in such probable $J = 0$ systems has sometimes been claimed to be due to the presence of $\text{Ir}^{4+}/\text{Ir}^{6+}$ impurity ions [13]. To confirm the oxidation state, XPS spectra for the Ir $4f$ core level [Fig. 2(a)] were collected and fitted by a single spin-orbit split doublet with separations of ~ 3.06 eV for the three systems. The energy positions of $4f_{7/2}$ and $4f_{5/2}$ in the doublets confirm the 5+ oxidation state of Ir [43]. In the conventional picture without the effect of SOC, this

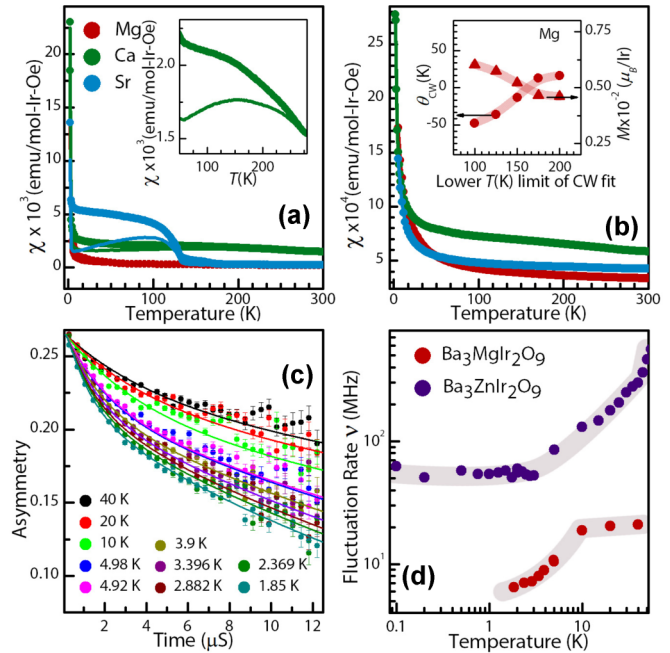


FIG. 3. Zero field cooled (thinner lines) and field cooled (thicker circles) magnetic susceptibilities measured with magnetic fields (a) 0.005 T and (b) 0.5 T for $\text{Ba}_3\text{M}\text{Ir}_2\text{O}_9$ ($M = \text{Mg}, \text{Ca}, \text{Sr}$). The inset to panel (a) shows the same curves for 0.005 T in enlarged form. The inset to panel (b) shows the θ_{CW} (circles) and effective magnetic moment per Ir (triangles) obtained for different temperature ranges of fitting the susceptibility data of $\text{Ba}_3\text{Mg}\text{Ir}_2\text{O}_9$ under 0.5 T field using the Curie-Weiss law. The x axis represents the lower temperature value to which each fitting has been done from 300 K. (c) Time evolutions of muon polarization and their fittings (continuous lines) for $\text{Ba}_3\text{Mg}\text{Ir}_2\text{O}_9$ in zero external field at different temperatures according to Eq. (1). (d) Fluctuation rate of the internal fields versus temperature obtained from the fitting for $\text{Ba}_3\text{Mg}\text{Ir}_2\text{O}_9$ and $\text{Ba}_3\text{Zn}\text{Ir}_2\text{O}_9$ [9].

oxidation state would allow four electrons in the t_{2g} orbitals, thereby forming a metallic system. To probe the metallicity we also collected the valence band photoemission spectra, and absence of density of states (DOS) at the Fermi level points towards a gapped electronic structure as shown in Fig. 2(b) for the compounds. The temperature dependence of electrical resistivity (ρ) of the three systems, measured by standard four probe method, is shown in Fig. 2(c), which corroborates the conclusion from valence band photoemission spectra.

In light of the above experimental observations, we have analyzed the electronic structure of these three systems. The characteristic feature of the electronic structure of these three pentavalent iridium compounds in absence of SOC and U is the isolated manifold of twelve t_{2g} bands arising from the four Ir atoms in the primitive unit cell across the Fermi level, making these systems metallic within GGA. Since the crystal field splitting is found to be high (~ 3 eV), and the Ir ions are in d^4 configuration, the Ir- t_{2g} states are partially filled and well separated from the completely empty e_g orbitals [40]. Hence, the entire physics of these systems is governed by the Ir- t_{2g} orbitals. The plots showing the nonmagnetic DOS for these compounds are presented in Fig. 3 of the SM [40]. While the Ir- t_{2g} bandwidths are found to be comparable (1.44, 1.2,

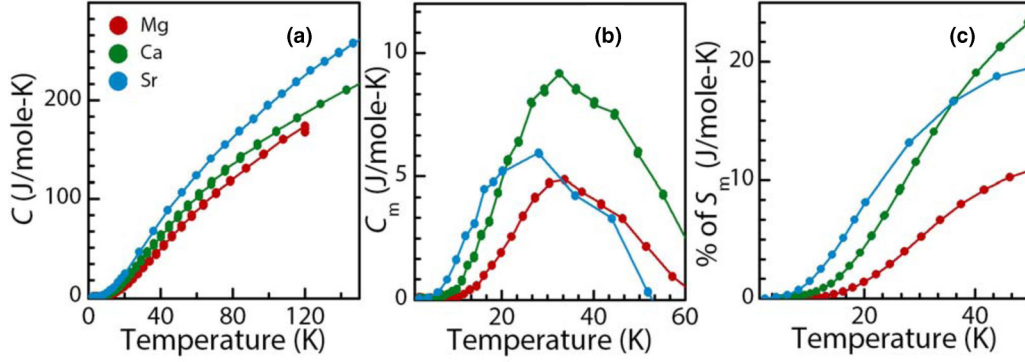


FIG. 4. Temperature dependence of (a) heat capacity (C), (b) magnetic heat capacity (C_m) after subtracting the lattice contribution, and (c) percentage magnetic entropy release for Ba₃MIr₂O₉ ($M = \text{Mg, Ca, Sr}$).

and 1.44 eV for Ba₃MgIr₂O₉, Ba₃CaIr₂O₉, and Ba₃SrIr₂O₉ respectively), no evidence of a charge gap is found in the absence of SOC and U , suggesting the importance of both SOC and U in driving these systems to be insulating. The similar values of bandwidth, however, suggest that the strength of SOC should be comparable in these compounds.

Next we investigated the nature of magnetism in these systems. DC magnetic susceptibility was measured under zero field cooled (ZFC) and field cooled (FC) protocols to probe the type of bulk magnetic properties of these materials. As can be seen from Fig. 3(a), the susceptibility of Ba₃MgIr₂O₉ measured under 0.005 T does not show any anomaly in the range of 2–300 K and resembles paramagnetic behavior. However, such featureless magnetic data from systems having small moments, without any long range order but possessing short range magnetic interactions, are often difficult to analyze using a Curie-Weiss law, since the parameters extracted from fitting vary with the range of temperatures chosen [44]. Thus we measured susceptibilities under a magnetic field of 0.5 T and fitted the data down to different temperatures from 300 K with the equation $\chi_0 + C_W/(T - \theta_{CW})$, where χ_0 is the temperature independent susceptibility, and C_W and θ_{CW} represent the Curie constant and Curie-Weiss temperature, respectively. The inset to Fig. 3(b) shows the extracted values of effective moment and θ_{CW} for different temperature ranges of fitting the data of Ba₃MgIr₂O₉. Naturally, it is not very realistic to

claim a definite θ_{CW} value in such cases. Still, a value of θ_{CW} in the range of -50 to -20 K and a moment of $\sim 0.5-0.6 \mu_B/\text{Ir}$ appears to be most reasonable. For Ba₃CaIr₂O₉, the ZFC and FC data for low magnetic field show a dimer-like (gapped) magnetic signature [inset to Fig. 3(a)], but is not clear in the 0.5 T magnetic data [Fig. 3(b)]. We could not fit the dimeric feature observed, using standard magnetic susceptibility expressions for dimers [45]. Taking two separate components, a Curie and a gapped dimer, also resulted in negligible spin gap, suggesting that the weak features may arise due to formation of intradimer singlets having very weak interaction strength. Surprisingly, for Ba₃SrIr₂O₉, a weak ferromagnetic feature is seen to be present at low field, which disappears on the application of a magnetic field of 0.5 T.

Thus hexagonal Ba₃MgIr₂O₉ only, due to its close structural similarity to spin-orbital liquid Ba₃ZnIr₂O₉, shows noticeable AFM interaction and a featureless magnetic susceptibility down to 2 K. In order to compare how the spins fluctuate as the temperature is lowered, to the case of Ba₃ZnIr₂O₉, we did muon spin relaxation (μSR) measurement in zero field, a technique perfectly suited to detect weak and/or partial freezing of local magnetic moments. The evolution of muon asymmetry for Ba₃MgIr₂O₉ down to 1.85 K is shown in Fig. 3(c). Upon lowering the temperature, the relaxation rate increases sharply from about 10 K as a result of slowing down of the spin fluctuations. Despite this slowing down of spin

TABLE I. Energy of various symmetry allowed magnetic states of Ba₃MgIr₂O₉ along with the spin and orbital moments within GGA+ U and GGA+SOC+ U approaches. The energy of the $P6_3/mm'c'$ magnetic space group is assumed to be zero. Orbital moments of Ir ions are written within the parentheses.

Magnetic configuration	Intradimer interaction	Interdimer interaction	GGA+ U			GGA+SOC+ U		
			$\Delta E/\text{f.u.}$ (meV)	Moment/Ir (μ_B)	Total moment/f.u. (μ_B)	$\Delta E/\text{f.u.}$ (meV)	Moment/Ir (μ_B)	Total moment/f.u. (μ_B)
$P6_3/mm'c'$	FM	FM	0.0	1.08	4	0.0	0.59 (0.08)	2.19
$P6'_3/m'm'c$	AFM	AFM	83	0.76	0.0	-68	0.71 (0.25)	0.0
$P6_3/mm'c$	FM	AFM	-5	0.96	0.0	10	0.61 (0.17)	0.0
$P6_3/m'm'c'$	AFM	FM	36	0.86	0	-60	0.73 (0.20)	0.0
$P6'_3/m'm'c', P6_3/mmc'$	NM	NM	187	0	0	28	0	0
$P6_3/m'mc, P6_3/mmc$								

TABLE II. The detailed spin component description of the symmetry allowed magnetic structures corresponding to the $C2/c$ space group, assuming the propagation vector $\mathbf{k} = (0,0,0)$.

Atom	$C2/c$	$C2/c'$	$C2'/c$	$C2'/c'$
1	(m_x, m_y, m_z)	(m_x, m_y, m_z)	(m_x, m_y, m_z)	(m_x, m_y, m_z)
3	$(-m_x, m_y, -m_z)$	$(-m_x, m_y, -m_z)$	$(m_x, -m_y, m_z)$	$(m_x, -m_y, m_z)$
2	(m_x, m_y, m_z)	$(-m_x, -m_y, -m_z)$	$(-m_x, -m_y, -m_z)$	(m_x, m_y, m_z)
4	$(-m_x, m_y, -m_z)$	$(m_x, -m_y, m_z)$	$(-m_x, m_y, -m_z)$	$(m_x, -m_y, m_z)$
5	(m_x, m_y, m_z)	(m_x, m_y, m_z)	(m_x, m_y, m_z)	(m_x, m_y, m_z)
7	$(-m_x, m_y, -m_z)$	$(-m_x, m_y, -m_z)$	$(m_x, -m_y, m_z)$	$(m_x, -m_y, m_z)$
6	(m_x, m_y, m_z)	$(-m_x, -m_y, -m_z)$	$(-m_x, -m_y, -m_z)$	(m_x, m_y, m_z)
8	$(-m_x, m_y, -m_z)$	$(m_x, -m_y, m_z)$	$(-m_x, m_y, -m_z)$	$(m_x, -m_y, m_z)$

dynamics, no spontaneous oscillation or “one-third” tail was observed that signifies magnetic transition to a frozen state [9]. As in $\text{Ba}_3\text{ZnIr}_2\text{O}_9$, the asymmetry can be decomposed into three contributions: one fast relaxing, one slower, and one hardly relaxing, most probably corresponding to three muon stopping sites located at increasing distance from the Ir moments. We therefore used the same minimal model as in Ref. [9],

$$A(t) = f_1 G(t, \Delta H_1, \nu) + f_2 G(t, \Delta H_2, \nu) + (0.265 - f_1 - f_2) K T(t, \Delta H), \quad (1)$$

where $K T$ is the Kubo-Toyabe function [46] accounting for the static nonrelaxing nuclear field distribution of width ΔH (0.5 MHz), f_1 (0.038) and f_2 (0.166) are the fractions of the two faster relaxing components, and $G(t, \Delta H, \nu)$ is the dynamical relaxation function [47], that takes into account the effect of a fluctuating field distribution of width ΔH at a rate ν . The fits with respect to this model are shown in Fig. 3(c), where only the fluctuation rate ν was allowed to vary with temperature. The extracted ν values are plotted in Fig. 3(d) together with that of $\text{Ba}_3\text{ZnIr}_2\text{O}_9$ [9]. The dynamical relaxation function can be used to the lowest measured temperature, since the inequality $\nu > \gamma \Delta H$, where $\gamma = 2\pi \times 135.5$ Mrad $\text{s}^{-1} \text{T}^{-1}$ is the muon gyromagnetic ratio, holds for both the relaxing components. At the lowest measured temperatures we obtain $\gamma \Delta H_1 = 1.59$ MHz and $\gamma \Delta H_2 = 0.35$ MHz and $\nu = 6.48$ MHz. It can be seen that, although there is considerable spin fluctuation present to 1.85 K, it is one order

less than that for $\text{Ba}_3\text{ZnIr}_2\text{O}_9$ and has a much steeper drop below 10 K. While we find noticeable AFM interactions from magnetic susceptibility, frustration for the Mg system seems to be much weaker compared to the Zn compound.

Since magnetic frustration can also be estimated by the amount of magnetic entropy retained by a material at very low temperatures, we measured heat capacity of all the three compounds, and the results are presented in Fig. 4(a). None of the three compounds show any anomaly in the heat capacity data corresponding to the features seen in the magnetic susceptibility for low fields. Although the hump-like behavior in $\text{Ba}_3\text{CaIr}_2\text{O}_9$ and ferromagnet-like upturn in $\text{Ba}_3\text{SrIr}_2\text{O}_9$ are seen at high temperatures (> 120 K) in magnetic susceptibilities, their absence in heat capacity suggest that these magnetic interactions are too weak. To extract the magnetic heat capacity C_m by subtracting the lattice contribution, C was also measured for nonmagnetic $\text{Ba}_3\text{ZnSb}_2\text{O}_9$. The difference of molecular weights between these compounds have been taken into account following the scaling procedure by Bouvier *et al.* [48]. The obtained C_m data from all the three compounds are plotted in Fig. 4(b) which shows a broad hump around ~ 20 – 40 K followed by a decay. With the application of external magnetic field as high as 9 T, no change in the heat capacity data was found, indicating absence of any paramagnetic impurity [49]. Despite having structure similar to $\text{Ba}_3\text{ZnIr}_2\text{O}_9$, $\text{Ba}_3\text{MgIr}_2\text{O}_9$ does not have any linear contribution to the magnetic heat capacity at low temperatures. The magnetic entropy obtained by integrating C_m/T with T is shown in Fig. 4(c). The percentage

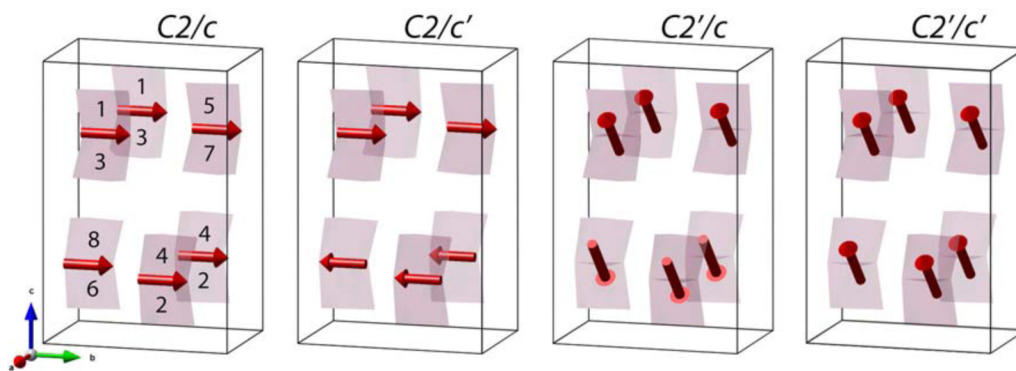

 FIG. 5. Spin alignment of the monoclinic ($C2/c$) symmetry allowed magnetic space groups, assuming the propagation vector $\mathbf{k} = (0,0,0)$ with the Ir ion number given corresponding to Table II [50]. The vectors represent the net spin direction of each Ir_2O_9 dimer.

TABLE III. Energy of symmetry allowed magnetic configurations along with the spin and orbital moments within the GGA+SOC+*U* approach for Ba₃CaIr₂O₉ and Ba₃SrIr₂O₉. The energy corresponding to the magnetic space group *C2/c* is assumed to be zero. Orbitals moments of Ir are written in the parentheses.

Magnetic configuration	Ba ₃ CaIr ₂ O ₉			Ba ₃ SrIr ₂ O ₉		
	ΔE /f.u. (meV)	Moment/Ir (μ_B)	Total moment/f.u. (μ_B)	ΔE /f.u. (meV)	Moment/Ir (μ_B)	Total moment/f.u. (μ_B)
<i>C2/c</i>	0.0	0.89 (0.30)	1.24	0.0	0.77 (0.22)	1.31
<i>C2/c'</i>	-22	0.88 (0.33)	0.0	84	0.69 (0.11)	0.0
<i>C2'/c</i>	5	0.88 (0.33)	0.0	33	0.85 (0.15)	0.0
<i>C2'/c'</i>	28	0.88 (0.31)	1.85	-21	0.79 (0.26)	-0.87

of magnetic entropy out of a maximum of $R \ln(2J + 1)$ with $J = 1$ that is released for Ba₃MgIr₂O₉ ($\sim 20\%$) is also much higher than that for Ba₃ZnIr₂O₉ ($\sim 7\%$) [9]. For the systems Ba₃CaIr₂O₉ and Ba₃SrIr₂O₉ the magnetic entropies released are even higher, consistent with the lesser frustrated *ab* planes that these systems have.

The variation in magnetic properties of these compounds must then result from their small structural differences. The *P6₃/mmc* symmetry of Ba₃MgIr₂O₉ allows eight possible magnetic space groups, assuming the magnetic unit cell to be the same as the crystallographic unit cell as given in Table I [50]. Total energy calculation shows that, among the considered configurations, the spin alignment corresponding to the magnetic space group *P6₃/m'm'c* (*P6₃/mm'c*) is lowest in energy with (without) the inclusion of SOC. It should be noted that only in the presence of SOC does the nature of intra-dimer exchange interaction in the lowest energy configuration change from FM to AFM, befitting the negative values of θ_{CW} from magnetic susceptibility experiments. Further, the calculated AFM isotropic exchange interactions indicate the presence of relatively stronger intradimer interaction ($J_1^{\text{ex}} = -21.3$ meV) compared to the interdimer exchange along the *c* direction ($J_2^{\text{ex}} = -1.4$ meV) and in the *ab* plane ($J_3^{\text{ex}} = -0.9$ meV). The stronger intradimer interaction is the result of direct exchange as well as superexchange interaction via the oxygen atoms, as revealed from the plot of the Wannier function [see Fig. 4 of the SM [40]]. Hence, the magnetic frustration is relatively weaker in Ba₃MgIr₂O₉ compared to its sister compound Ba₃ZnIr₂O₉

[9], which is also evident from the μ SR and heat capacity measurements.

In contrast, stronger distortions in the IrO₆ octahedra of Ba₃CaIr₂O₉ and Ba₃SrIr₂O₉ introduce different Ir-O-Ir angles [see Fig. 1(f)] which break the local inversion symmetry and give rise to uncompensated nearest neighbor Dzyaloshinskii-Moriya (DM) interactions, which can then cause canting of spins resulting in noncollinear magnetic structures. The monoclinic (*C2/c*) symmetry of these two systems allows four magnetic space groups, assuming the propagation vector $\mathbf{k} = (0, 0, 0)$: (a) *C2/c*, (b) *C2/c'*, (c) *C2'/c*, and (d) *C2'/c'* [50]. The details of these magnetic space groups are provided in Table II and the net spin direction (sum of the individual canted spins at the two iridium atoms within the dimer) of each dimer is shown in Fig. 5. The total energies for Ba₃CaIr₂O₉ and Ba₃SrIr₂O₉ corresponding to these allowed magnetic configurations in the presence of SOC are presented in Table III. For Ba₃CaIr₂O₉, magnetic configuration *C2/c'* is lowest in energy; each of the dimers carry net (spin-orbital) moments that are then aligned parallel to each other in the *ab* plane and antiparallel in the *c* direction (see Fig. 5). The weak dimeric feature observed in the magnetic susceptibility may be an outcome of this antiparallel interdimer arrangement of moments. Note that the intradimer interaction can also be AFM. In fact, in the *C2/c'* magnetic configuration the NN spin components are antiparallel except for the *y* component, which is probably due to canting. In Ba₃SrIr₂O₉, the lowest energy magnetic configuration is found to be *C2'/c'* (Fig. 5), where the net moments of each of the

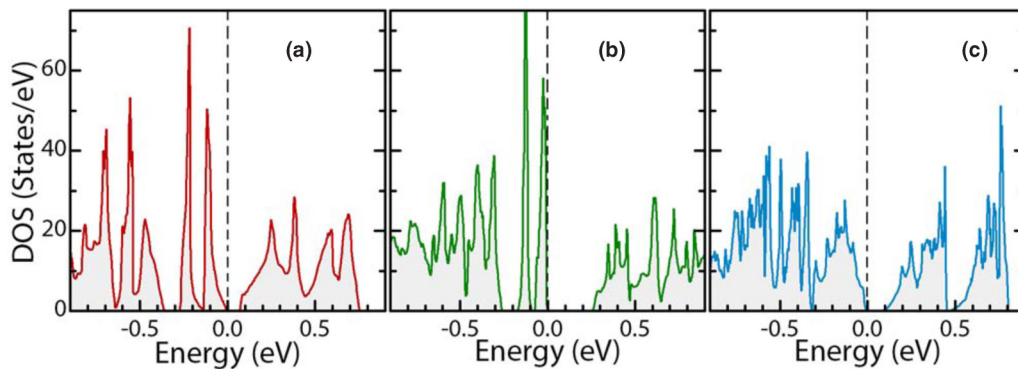


FIG. 6. The density of states (DOS) within GGA+SOC+*U* corresponding to the theoretically obtained magnetic ground state of (a) Ba₃MgIr₂O₉, (b) Ba₃CaIr₂O₉, and (c) Ba₃SrIr₂O₉.

Ir_2O_9 dimers are aligned parallel to each other, consistent with the observation of a ferromagnetic-like signature in magnetic susceptibility under low magnetic fields. The densities of states corresponding to the obtained magnetic ground states of these three systems are presented in Fig. 6. An insulating gap opens up only in the presence of SOC and U and has values of 63, 254, and 70 meV for $\text{Ba}_3\text{MgIr}_2\text{O}_9$, $\text{Ba}_3\text{CaIr}_2\text{O}_9$, and $\text{Ba}_3\text{SrIr}_2\text{O}_9$ respectively, in agreement with the insulating behavior obtained from experiments.

In conclusion, we find that spin-orbital moments, which are generated through mixing of J states as a result of the hopping induced superexchange mechanism between closely placed Ir^{5+} ions in Ir_2O_9 dimers, behave differently under application of external magnetic fields as a consequence of local variations in Ir-O-Ir exchange pathways. Therefore, while $\text{Ba}_3\text{MgIr}_2\text{O}_9$ having a $P6_3/mmc$ symmetry does not order until reaching 1.85 K despite having noticeable AFM exchange interactions, $\text{Ba}_3\text{CaIr}_2\text{O}_9$ shows weak dimer-like features and stabilizes in $C2/c'$ magnetic configuration with no net moment. On the other hand, $\text{Ba}_3\text{SrIr}_2\text{O}_9$ has a ground state corresponding to the magnetic space group $C2'/c'$ and exhibits weak ferromagnet-like features.

ACKNOWLEDGMENTS

A.N. and S.B. thank the Indian Association for the Cultivation of Science (IACS) and the Council of Scientific & Industrial Research (CSIR), India, respectively, for support via fellowships. S.R. thanks the Department of Science and Technology (DST) (Project No. WTI/2K15/74) for funding, and acknowledges financial support by the Indo-Italian Program of Cooperation, the Saha Institute of Nuclear Physics, the Collaborative Research Projects of Materials and Structures Laboratory at Tokyo Institute of Technology (TiTech), and the Newton-India fund. S.R. is also grateful for experiments performed at Elettra (Proposal No. 20140355), TiTech, and ISIS. Authors thank the Department of Science and Technology, India for the financial support, Saha Institute of Nuclear Physics and Jawaharlal Nehru Centre for Advanced Scientific Research, India for facilitating the experiments at the Indian Beamline, Photon Factory, KEK, Japan. F.B. acknowledges financial support from project SOCRATE (ANR-15-CE30-0009-01) of the French National Research Agency. S.R. and I.D. thank Technical Research Centre, IACS, Department of Science and Technology (DST), Government of India for support.

-
- [1] B. J. Kim, H. Jin, S. J. Moon, J.-Y. Kim, B.-G. Park, C. S. Leem, J. Yu, T. W. Noh, C. Kim, S.-J. Oh, J.-H. Park, V. Durairaj, G. Cao, and E. Rotenberg, *Phys. Rev. Lett.* **101**, 076402 (2008).
- [2] M. MorettiSala, V. Schnells, S. Boseggia, L. Simonelli, A. Al-Zein, J. G. Vale, L. Paolasini, E. C. Hunter, R. S. Perry, D. Prabhakaran, A. T. Boothroyd, M. Krisch, G. Monaco, H. M. Rønnow, D. F. McMorrow, and F. Mila, *Phys. Rev. B* **92**, 024405 (2015).
- [3] J. Reuther, R. Thomale, and S. Rachel, *Phys. Rev. B* **90**, 100405(R) (2014).
- [4] W. Witczak-Krempa, G. Chen, Y. B. Kim, and L. Balents, *Annu. Rev. Condens. Matter Phys.* **5**, 57 (2014).
- [5] J. G. Rau, E. K.-H. Lee, and H.-Y. Kee, *Annu. Rev. Condens. Matter Phys.* **7**, 195 (2016).
- [6] T. Sato, T. Shirakawa, and S. Yunoki, *Phys. Rev. B* **91**, 125122 (2015).
- [7] S. J. Moon, H. Jin, K. W. Kim, W. S. Choi, Y. S. Lee, J. Yu, G. Cao, A. Sumi, H. Funakubo, C. Bernhard, and T. W. Noh, *Phys. Rev. Lett.* **101**, 226402 (2008).
- [8] B. J. Kim *et al.*, *Science* **323**, 1329 (2009).
- [9] A. Nag, S. Middey, S. Bhowal, S. K. Panda, R. Mathieu, J. C. Orain, F. Bert, P. Mendels, P. G. Freeman, M. Mansson, H. M. Ronnow, M. Telling, P. K. Biswas, D. Sheptyakov, S. D. Kaushik, V. Siruguri, C. Meneghini, D. D. Sarma, I. Dasgupta, and S. Ray, *Phys. Rev. Lett.* **116**, 097205 (2016).
- [10] G. Chen and L. Balents, *Phys. Rev. B* **84**, 094420 (2011).
- [11] G. Cao, T. F. Qi, L. Li, J. Terzic, S. J. Yuan, L. E. DeLong, G. Murthy, and R. K. Kaul, *Phys. Rev. Lett.* **112**, 056402 (2014).
- [12] M. A. Laguna-Marco, P. Kayser, J. A. Alonso, M. J. Martínez-Lope, M. van Veenendaal, Y. Choi, and D. Haskel, *Phys. Rev. B* **91**, 214433 (2015).
- [13] T. Dey *et al.*, *Phys. Rev. B* **93**, 014434 (2016).
- [14] M. Bremholm, S. E. Dutton, P. W. Stephens, and R. J. Cava, *J. Solid State Chem.* **184**, 601 (2011).
- [15] G. Khaliullin, *Phys. Rev. Lett.* **111**, 197201 (2013).
- [16] J. Vallin, *Phys. Rev. B* **2**, 2390 (1970).
- [17] G. Chen, L. Balents, and A. P. Schnyder, *Phys. Rev. Lett.* **102**, 096406 (2009).
- [18] X. Liu, *et al.*, *Phys. Rev. Lett.* **109**, 157401 (2012).
- [19] S. Bhattacharjee, S.-S. Lee, and Y. B. Kim, *New J. Phys.* **14**, 073015 (2012).
- [20] C. H. Kim, H. S. Kim, H. Jeong, H. Jin, and J. Yu, *Phys. Rev. Lett.* **108**, 106401 (2012).
- [21] T. Dodds, T. P. Choy, and Y. B. Kim, *Phys. Rev. B* **84**, 104439 (2011).
- [22] G. Jackeli and G. Khaliullin, *Phys. Rev. Lett.* **103**, 067205 (2009).
- [23] D. I. Khomskii, K. I. Kugel, A. O. Sboychakov, and S. V. Streltsov, *J. Exp. Theor. Phys.* **122**, 484 (2016).
- [24] S. Bhowal, S. Baidya, I. Dasgupta, and T. Saha-Dasgupta, *Phys. Rev. B* **92**, 121113(R) (2015).
- [25] A. Nag *et al.* [arxiv:1707.09304](https://arxiv.org/abs/1707.09304).
- [26] C. Svoboda, M. Randeria, and N. Trivedi, *Phys. Rev. B* **95**, 014409 (2017).
- [27] K. I. Kugel, D. I. Khomskii, A. O. Sboychakov, and S. V. Streltsov, *Phys. Rev. B* **91**, 155125 (2015).
- [28] T. Sakamoto, Y. Doi, and Y. Hinatsu, *J. Solid State Chem.* **179**, 2595 (2006).
- [29] R. D. Shannon, *Acta Crystallogr. Sect. A* **32**, 751 (1976).
- [30] J. Rodríguez-Carvajal, *Physica B (Amsterdam)* **192**, 55 (1993).
- [31] K. Momma and F. Izumi, *J. Appl. Crystallogr.* **44**, 1272 (2011).
- [32] P. E. Blöchl, *Phys. Rev. B* **50**, 17953 (1994).
- [33] G. Kresse and D. Joubert, *Phys. Rev. B* **59**, 1758 (1999).
- [34] G. Kresse and J. Hafner, *Phys. Rev. B* **47**, 558(R) (1993).

- [35] G. Kresse and J. Furthmüller, *Phys. Rev. B* **54**, 11169 (1996).
- [36] V. I. Anisimov, J. Zaanen, and O. K. Andersen, *Phys. Rev. B* **44**, 943 (1991).
- [37] O. K. Andersen and T. Saha-Dasgupta, *Phys. Rev. B* **62**, R16219(R) (2000).
- [38] O. K. Andersen, T. Saha-Dasgupta, R. W. Tank, C. Arcangeli, O. Jepsen, and G. Krier, in *Electronic Structure and Physical Properties of Solids: The Uses of the LMTO Method*, edited by H. Dreysse, Lecture Notes in Physics (Springer, Berlin, 2000), p. 3.
- [39] O. K. Andersen, T. Saha-Dasgupta, and S. Ezhov, *Bull. Mater. Sci.* **26**, 19 (2003).
- [40] See Supplemental Material at <http://link.aps.org/supplemental/10.1103/PhysRevB.97.064408>, which includes Refs. [28,41,42] and details of the structural refinement parameters, EXAFS results, plots of non-magnetic DOS for the three systems, Wannier function plot for Ba₃MgIr₂O₉, and Longitudinal-field μ SR results for Ba₃MgIr₂O₉.
- [41] S. Middey, S. Ray, K. Mukherjee, P. L. Paulose, E. V. Sampathkumaran, C. Meneghini, S. D. Kaushik, V. Siruguri, K. Kovnir, and D. D. Sarma, *Phys. Rev. B* **83**, 144419 (2011).
- [42] C. Meneghini, S. Ray, F. Liscio, F. Bardelli, S. Mobilio, and D. D. Sarma, *Phys. Rev. Lett.* **103**, 046403 (2009).
- [43] Y. Shimizua, S. Takasea, and T. Otsuoa, *ECS Trans.* **3**, 263 (2006).
- [44] A. Nag and S. Ray, *J. Magn. Magn. Mater.* **424**, 93 (2017).
- [45] L. Shlyk, K. Nenkov, B. Schüpp-Niewa, G. Krabbes, and G. Fuchs, *Phys. Rev. B* **74**, 054428 (2006).
- [46] R. S. Hayano, Y. J. Uemura, J. Imazato, N. Nishida, T. Yamazaki, and R. Kubo, *Phys. Rev. B* **20**, 850 (1979).
- [47] A. Keren, *Phys. Rev. B* **50**, 10039 (1994).
- [48] M. Bouvier, P. Lethuillier, and D. Schmitt, *Phys. Rev. B* **43**, 13137 (1991).
- [49] J. M. Schliesser and B. F. Woodfield, *Phys. Rev. B* **91**, 024109 (2015).
- [50] J. M. Perez-Mato, S. V. Gallego, E. S. Tasci, L. Elcoro, G. de la Flor, and M. I. Aroyo, *Annu. Rev. Mater. Res.* **45**, 217 (2015).